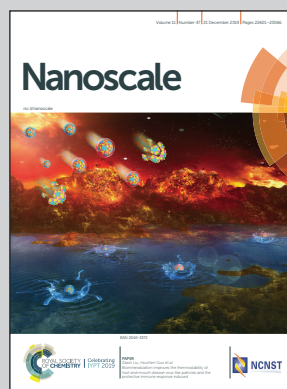


Showcasing research from Prof. Hsueh-Chia Chang's group at the University of Notre Dame, Indiana, USA.

Biphasic signals during nanopore translocation of DNA and nanoparticles due to strong ion cloud deformation

At high field strengths, the ionic cloud surrounding nanocolloids and biomolecules may become strongly deformed, leading to a gradient in local ion conductivity in the field direction. This phenomenon manifests itself as a biphasic current signature during translocation through a nanopore, characterized by an initial dip in current during entry due to volume exclusion and followed by an overshoot over the base line due to an increase in the pore conductance by the deformed ion cloud of the departing particle.

As featured in:



See Hsueh-Chia Chang et al.,
Nanoscale, 2019, **11**, 22772.

Cite this: *Nanoscale*, 2019, **11**, 22772

Received 19th June 2019,
Accepted 21st August 2019
DOI: 10.1039/c9nr05223b
rsc.li/nanoscale

Biphasic signals during nanopore translocation of DNA and nanoparticles due to strong ion cloud deformation

Sebastian Sensale, ^a Zhangli Peng^a and Hsueh-Chia Chang ^{*a,b}

We report a theory for biphasic ionic current signals during DNA and nanoparticle translocation through a solid-state nanopore that produces scaling results consistent with those of finite element simulations (FEM), molecular dynamics (MD) simulations and experiments. For standard nanopores designed for potential rapid sequencing applications, the electric field is enhanced by orders of magnitude due to field focusing and can severely deform the ion-cloud around the charged DNA. Highly fore-aft asymmetric space charge distribution leads to a universal quasi-steady comet-like structure with a long tail. In contrast to previous biphasic theories, the charge density and length of the tail, which are responsible for the negative resistive pulse, are shown to depend sensitively on the dimensionless applied field, the Peclet number Pe , with a ∓ 1 scaling, due to a balance between tangential migration and normal diffusion. An optimum Pe is predicted where the negative pulse has the maximum amplitude.

Introduction

Solid-state nanopores (3–100 nm in diameter) allow a much higher throughput for DNA translocation than 1.5 nm protein nanopores¹ and this is suggested as a better nanopore technology than that of soft protein nanopores for sequencing, bio-sensing and molecular memory applications. However, the faster translocation comes with highly transient and complex ionic current signals that have so far defeated any attempt to decipher the sequence or even the length of the DNAs. Some recent attempts that use surface modification and corner field pinning can decipher the difference between short (~20 base) single-stranded and double-stranded nucleic acids, but only if other nucleic acids have been removed.^{2,3} The key reason why larger solid-state nanopores produce far more complex ion current dynamics than their smaller (and shorter) protein counterparts is the distortion of the ion cloud around the highly charged DNA by the focused applied electric field. For spherical colloids, it is known that a highly distorted ion cloud can produce a negative resistive pulse.^{4–7} This negative pulse is typically preceded by a positive resistive pulse, resulting in a biphasic resistive signal. Similar biphasic signals have been observed for DNA translocation.⁸ A theory for such a biphasic signal for DNA translocation through a solid state nanopore

has been advanced by Das *et al.*,⁹ although it is based on external concentration polarization by the ion-selective DNA-pore gap rather than distortion of the DNA ion cloud, with a very different description of the biphasic signal that is sensitive to the pore surface charge density and cannot explain biphasic signals by spherical nanocolloids or the most common solid-state nanopores at common DNA buffers, with a gap size much larger than the Debye length. There are other potential mechanisms for complex ion current dynamics during molecular translocation through large solid-state nanopores, such as adsorption/desorption and DNA conformation changes within the pore,^{10,11} but these mechanisms do not contribute to the unique biphasic signals. In this article, we report the first scaling theory for the distortion of the ion cloud around a linear DNA molecule, due to electrophoretic distortion of the counterion cloud, by the high field in the pore and without electrostatic interaction with the solid-state nanopore, and show that the closed-form estimate is in good agreement with finite element simulations (FEM), molecular dynamics (MD) simulations and experimental data. It also predicts an optimum applied field for the maximum amplitude of the biphasic signal, which is confirmed by numerical simulations.

Results

Boundary layer theory

Consider a dielectric cylinder (our model for DNA, as seen in Fig. 1) with a uniform surface charge density Σ , radius a and

^aDepartment of Aerospace and Mechanical Engineering, University of Notre Dame, Notre Dame, Indiana 46556-5637, USA. E-mail: hchang@nd.edu

^bDepartment of Chemical and Biomolecular Engineering, University of Notre Dame, Notre Dame, Indiana 46556-5637, USA

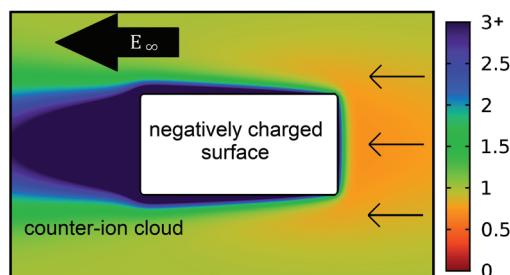


Fig. 1 Distribution of counter-ion concentration C/C_∞ surrounding a negatively charged cylindrical particle moving in an electric field $E_\infty = 8.33 \times 10^7 \text{ V m}^{-1}$ ($C_\infty = 0.01 \text{ M}$) obtained from finite element method (FEM) simulations. ($L = 22.44 \text{ nm}$, $\Sigma = 0.0275 \text{ C m}^{-2}$, $a = 5.925 \text{ nm}$).

length L immersed in a symmetric univalent electrolyte solution with an ionic concentration C_∞ at large distances from the particle, ionic diffusion coefficient D , and permittivity ϵ . As is true of all boundary layer theories, ours is valid for molecules of any geometry, so long that their macroscopic length scale L is much larger than their boundary layer thickness ($\text{Pe} \gg 1$), but we will present our results for a cylindrical rod for simplicity.

There is considerable debate on the surface charge density of the translocating DNA. For translocation through protein nanopores, particularly with unzipping action, a very low charge density of $0.1e^-$ per base has been reported.^{12,13} This charge density seems to be a strong function of the ionic strength and the specific protein nanopores,^{10,13–16} due to the interaction between the DNA and the protein, particularly for the much more flexible single-stranded fragments. However, for larger solid-state nanopores, there seems to be a consensus of $0.5e^-$ charge density for double-stranded DNAs that is independent of pore dimension and ionic strength.^{1,17} This effective charge density is consistent with the classical Manning condensation theory for compensation of a cylinder by counter-ions,¹⁸ given the bare DNA charge density of $2e^-$ for completely dissociated phosphate functional groups. We will hence focus on the translocation of double-stranded DNAs through solid-state nanopores and will validate our theory for effective charge densities ranging from 0.5 to $2e^-$.

Upon exposure of the system to an external electric field E_∞ , ions far from the particle move with a uniform velocity, $u = (DF/RT)E_\infty$, where F is the Faraday constant, R is the gas constant and T is the temperature of the system.¹⁹ (Since we will be considering a thin boundary layer theory for the space charge, the same theory applies for a sphere by simply replacing both a and L by the radius and diameter of the sphere, modulo a universal constant, as is consistent with the classical advection-diffusion boundary layer theory. Other molecular geometries also yield the same results.) After the axis of the DNA molecule aligns with the electric field,²⁰ the external field E_∞ becomes tangent to the cylinder and begins to disrupt the Boltzmann equilibrium within the Debye layer around the cylinder. This equilibrium is established when normal diffusive flux of both ions is equal to their respective normal

electromigration flux due to the surface field $E_s = \Sigma/\epsilon$, resulting in no temporal variation in either ion concentration. The largest possible surface field for an uncompensated double-stranded DNA molecule, with a bare charge of $2e^-$ (electrons) per base pair, is $\sim 0.15 \text{ V nm}^{-1}$ after accounting for the cylindrical geometry. When the Debye length λ_D is much smaller than the DNA radius a , the space charge density in the equilibrium Debye layer decays exponentially to zero away from the surface even when the Debye–Hückel linearization cannot be applied.²¹ Hence, the surface field is screened accordingly, and the normal field also decays exponentially towards the bulk over a length scale corresponding to the Debye slip length $\lambda_D = \sqrt{\epsilon RT/2F^2C_\infty}$. As such, the tangential electromigration becomes much larger than the normal electromigration at the outer boundary of the Debye layer. Near the surface, however, the surface field still dominates within a Stern length of about $RT/FE_s \approx 0.17 \text{ nm}$.²¹ Consequently, the highly conductive Stern layer becomes a source-like layer for the boundary layer outside it, with both within the original Debye layer. The thinness of the boundary layer stipulates that the normal diffusive flux remains dominant over the tangential diffusive flux. Consequently, the non-equilibrium “diffusion” boundary layer is the one determined by a balance between tangential migration and normal diffusion. The tangential flux “downstream” (following the electromigration flux surrounding the particle) increases the thickness of the boundary later at the tail of the particle, where charges accumulate. This gradient in ionic charge density produces a highly distorted and thin boundary layer ion cloud around the cylinder, as shown in Fig. 1.

For a symmetric electrolyte, the Nernst–Planck equations of the two ions can be transformed into two equivalent equations for the local conductivity σ and mobile ionic charge density ρ ^{19,21} in an inertial referential frame moving with the DNA,

$$D\nabla^2\rho = \vec{u}\nabla\rho - \nabla\cdot(\sigma\nabla\phi), \quad (1)$$

$$D\nabla^2\sigma = \vec{u}\nabla\sigma - \left(\frac{DFz'}{RT}\right)^2 \nabla\cdot(\rho\nabla\phi). \quad (2)$$

where $\vec{u} = \mu\vec{E}_\infty$ is the electrophoretic velocity of the DNA with electrophoretic mobility μ . For molecules with large enough surface charge densities, the EDL is mostly formed by counter-ions and hence the conductivity can be related to the charge density $\sigma_b \approx DFz'\rho/RT$, $\rho \approx Fz'C_+$. As a result, these two equations reduce to one equation for the mobile charge density

$$D\nabla^2\rho = \vec{u}\nabla\rho - \left(\frac{DFz'}{RT}\right)\nabla\cdot(\rho\nabla\phi). \quad (3)$$

Upon exposure of the system to an external electric field \vec{E}_∞ tangent to the molecule, counter-ions far from the surface move with uniform velocities $(DFz'/RT)\vec{E}_\infty$ while the DNA molecule moves in the opposite direction with a velocity $\mu\vec{E}_\infty$. These velocities are parallel and antiparallel to the longitudinal z direction, with the ion velocity being much higher than the DNA velocity. Due to the slenderness of the boundary layer at a large Peclet number and for a slender molecule $L \gg a$ (see

Fig. 1), the gradient in the mobile charge density is mostly in the radial direction r . At the outer edge of the boundary layer, the external field is much larger than the normal field due to the surface charge and the external field remains constant such that $\nabla^2\phi = 0$. Hence, in the frame moving with the DNA, the final screening term in the above equation becomes $(DFz'/RT)E_\infty(\partial\rho/\partial z)$ and, using the local Cartesian coordinate to simplify $\nabla^2\rho \sim \partial^2\rho/\partial r^2$, we obtain

$$D \frac{\partial^2 \rho}{\partial r^2} = \tilde{u} \frac{\partial \rho}{\partial z}. \quad (4)$$

The typical Debye screening term of a one-dimensional Nernst–Planck equation that arises from normal electromigration has been replaced by a tangential electromigration term by the external field, with the velocity now containing both the electrophoretic velocity of the counterion and the DNA, $\tilde{u} = (DFz'/RT)E_\infty + \mu E_\infty$. The ion velocity is typically much larger than the DNA velocity. As a result, instead of a Boltzmann equilibrium between diffusion and normal (radial) electromigration, we have a non-equilibrium steady state between radial diffusion and tangential electromigration in the diffusion boundary layer. Closer to the surface, the normal field is higher than the tangential field and a one-dimensional Boltzmann equilibrium exists in the inner Stern layer. Counter ions are fed into this inner layer continuously from the tip of the DNA to maintain this Boltzmann equilibrium. The counter-ions in the inner Stern layer then diffuse through the diffusion boundary layer and are convected to the tail region as governed by (4). These two regions are “matched” in the subsequent analysis.

Because the applied external field is much larger than the normal field by the surface charge in the diffusion boundary layer, the tangential field is not screened and \tilde{u} is position independent. The distance z along the axis of the particle takes values from $z = 0$ (the depleted front of the cylinder) to $z = L$ (the downstream enriched end). Electro-osmotic and curvature effects are neglected due to the thin boundary layer with a thickness much smaller than the Debye hydrodynamic slip length.

Since the tangential field E_∞ is much larger than the screened normal field due to the charge, its screening by the charge in the diffusion layer is negligible and the convection velocity \tilde{u} is a constant independent of position. Consequently, the classical “free-surface” boundary-layer analysis can then be applied for high Peclet numbers $\text{Pe} = \tilde{u}L/D \gg 1$. A simple scaling shows that the width of this layer varies downstream as $\delta(z) \sim (zL/\text{Pe})^{1/2}$. We also observe that the advection-diffusion equation yields a self-similar solution $\rho = f(\omega)$ with $\omega = (r - a)/\delta(z)$, leading to an analytical expression for the space charge density ρ in the surrounding of the cylinder,

$$\rho(r, z) = \frac{\delta(z)\Sigma}{\lambda_D^2} \left[1 - \text{erf} \left(\frac{r - a}{2\delta(z)} \right) \right] \quad (5)$$

for $r \geq a$ and $z \in [0, L]$, where erf is the error function $\text{erf}(x) = \frac{1}{\sqrt{\pi}} \int_{-x}^x \exp(-t^2) dt$. We have used the electroneutral conditions in the bulk, $\rho(r \rightarrow \infty) = 0$, as well as the Debye–

Hückel approximation for the charged diffusion layer due to the thinness of the boundary layer at large Peclet numbers. As the diffusion layer still shows a balance between diffusion and electromigration, although the latter is now in the tangential direction, a quasi-Boltzmann equilibrium distribution still exists within it which, in the Debye–Hückel limit, can be expressed as $\rho \sim -\phi e/\lambda_D^2$. The electric potential ϕ is the potential within the diffusion layer and its value at the surface $\phi(a, z)$ represents the normal potential drop across the charged diffusion layer at a particular position z . Because the Debye–Hückel approximation can be made within the diffusion layer, this surface potential can be related to the surface field due to the surface charge (or effective surface field due to Stern layer screening), $\phi(a, z) = E_s \delta(z)$. This matching then determines the space charge density at the surface boundary of the diffusion layer in (5),

$$\rho(a, z) \sim \frac{E_s \delta(z) \epsilon}{\lambda_D^2} = \frac{\sum \delta(z)}{\lambda_D^2}, \quad (6)$$

which is in good agreement with the numerical data in the large applied field limit ($\text{Pe} > 20$) shown in Fig. 2A. We note in Fig. 2A that the simulated surface space charge density undergoes a discontinuous change when Pe is below 20. The classical Debye layer Boltzmann equilibrium with an opposite scaling (independence) with respect to the applied field appears below this critical Pe . The charged diffusion boundary layer and the tail it produces hence appear abruptly beyond a critical Pe .

Integrating the space charge density from (5) along the length of the cylinder, the net space charge surrounding the cylinder can be estimated through:

$$q_s = \int_0^L \int_0^{2\pi} \int_a^{+\infty} \rho(r, z) r dr d\theta dz \sim q_p \left[\text{Pe} \left(\frac{\lambda_D}{L} \right)^2 \right]^{-1}, \quad (7)$$

where q_p is the total charge of the cylinder $q_p = 2\pi a L \Sigma$ and the universal pre-factor is estimated to be ≈ 0.65 . Since q_s must be smaller than q_p , we are restricted to the limit of $\text{Pe}(\lambda_D/L)^2 \gg 1$. The key Pe^{-1} scaling arises because the space charge density ρ scales proportional to the diffusion layer thickness in (6), $\rho \sim \delta \sim L \text{Pe}^{-1/2}$, and the total space charge around the cylinder requires integration of this density over the polarized diffusion layer thickness, where $r dr - adr$ in the thin layer high- Pe limit. The net space charge around the cylinder decreases with the electric field as Pe^{-1} , as the counter-ions are convected to the tail by electromigration. The agreement of this asymptotic approximation with the numerically evaluated q_s is illustrated in Fig. 2B. MD simulations can only resolve up to $\text{Pe}(\lambda_D/L)^2 \sim O(1)$ but they are consistent with the numerical data in that region, which generates data for $\text{Pe}(\lambda_D/L)^2 \gg 1$ that is well fitted by (7).

The space charge on the cylinder (7) suggests that electroneutrality is not achieved in $z \in [0, L]$ and thus a tail of counter-ions with charge $q_p - q_s$ will lag behind the particle. In the tail region, without the charge source from the Stern layer, there is no diffusion in the normal direction and the infinite Pe limit of (4) stipulates that the space charge density is uniform in the

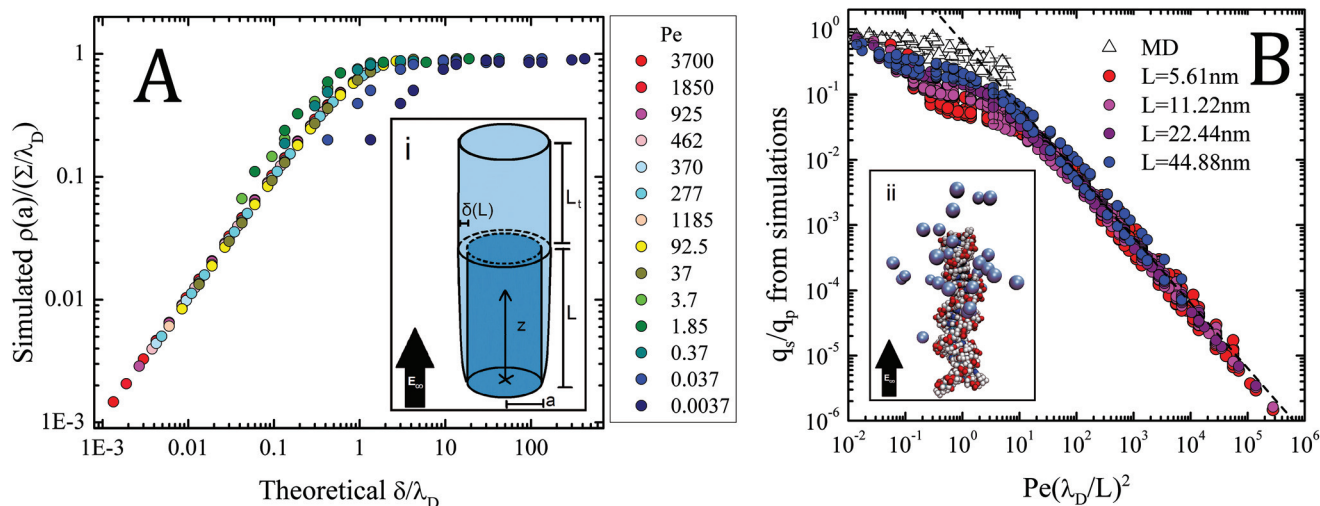


Fig. 2 (A) Space charge density ρ evaluated at the surface of the cylinder from FEM simulations as a function of the theoretical $\delta(z)/\lambda_D$. Ionic strengths were varied from 0.1 mM to 1 M and external field amplitudes were varied from 8 kV m^{-1} to 8 V nm^{-1} . $\Sigma = 0.0275 \text{ C m}^{-2}$, $a = 1.185 \text{ nm}$, and $L = 11.22 \text{ nm}$ and ρ was evaluated at $z = L/2$. (B) Normalized screening charge q_s/q_p surrounding the cylinder ($z \in [0, L]$) obtained from FEM simulations (circles) for $a \in \{1.185, 2.37, 5.925\} \text{ nm}$, $\Sigma \in \{0.0275, 0.055, 0.11, 0.22\} \text{ C m}^{-2}$ and ionic strengths and external field amplitudes correspond to the diffusion-layer scaling regions of (A). The dotted line is our high Peclet estimate from (4). Triangles represent the normalized screening charge surrounding a double stranded DNA molecule with 22 base-pairs from molecular dynamics (MD) simulations for molar strengths 0.01, 0.05, 0.1, 0.5 and 1 M and external fields E_∞ from 0.01 to 1 V nm^{-1} .

tail. Imposing continuity of the flux of counter-ions at the end of the cylinder, $\tilde{\rho}(a,L)[(a + \delta(L))^2 - a^2] \approx \tilde{\rho}(r,z)a^2$ for $z \geq L$ and $r \leq a + \delta(L)$, the space charge density at the end of the cylinder can be estimated through $\rho(r,z) \approx \rho(a,L)2\delta(L)/a \sim 2(\Sigma/a)(L^2/\lambda_D^2)$ for $z \geq L$. In the thin layer high-Pe limit, the cylindrical tail has a radius of a and a simple global electroneutrality constraint, $q_p = q_s + q_t$ where q_t is the net charge in the tail, providing an estimate for the tail length $L_t \sim (\lambda_D^2/L)\text{Pe}$. At high Pe, L_t/L is much larger than unity and the tail of the DNA comet is much longer than the DNA length, as most of the charge is swept into the tail even when the tail charge density decreases.

Biphasic signals in nanopores

Two competing effects dominate the conductance during DNA and nanoparticle translocation in nanopores: the volume exclusion of ions in the pore by the translocating entity, which decreases the conductivity, and the introduction of new ions brought into the pore by its respective ionic cloud, which increases the conductance.⁵ Nanoparticles with a low surface charge do not bring a large number of counter-ions. Thus, volume exclusion dominates the whole resistive pulse and the particle size can be characterized from a drop in the current.⁴ Particles with a higher surface charge and with a large surface charge to volume ratio bring a larger number of counter-ions. Thus, depending on the number of charge carriers already inside the pore, the translocation event can either decrease or increase the ionic current above the baseline.^{1,6} It is typically assumed that these effects are independent of the electric field.⁵ However, as previously shown, high electric fields can alter the distribution of ions surrounding a DNA or nanoparticle significantly, leading to a field-dependent number of counter-ions inside the pore and

affecting the magnitude of the entire resistive pulse.^{4,5,7} At high field $\text{Pe} \gg 1$, most of the counter-ions around the DNA are swept into the tail and the tail is responsible for increasing the conductance of the pore to produce the negative resistive pulse into the tail and the tail is responsible for increasing the conductance of the pore to produce the negative resistive pulse at the end of the biphasic signal (see Fig. 3).

This positive peak has been predicted to occur in cases where the thickness of the electrical double layer of a DNA or nanoparticle is comparable to the pore dimensions^{9,10} such that the Debye layer of the DNA overlaps with the Debye layer of the surface to form an ion-selective annular region. However, recent experiments and simulations have shown that this condition is not necessary for its existence.^{4,7,8} The positive peak occurs even for large nanopores at high ionic strengths when the two Debye layers do not overlap. Hence, it must be a result of ion cloud distortion by the external field.

Hence, we focus on this negative resistance region by assuming that the DNA has exited the pore and only the tail remains. This allows us to omit the volume exclusion effect and only focus on how the tail of the counter-ions enhance the pore conductance. Under these conditions, the resistance inside a pore of length L_p and radius $r_p \gg a + \lambda_D$ with a negligible surface charge can be written as²² $R = 2R_{\text{access}} + R_{\text{channel}}$, where the access resistance R_{access} at the ends of the pore can be estimated through $1/4\sigma_p r_p$. This access resistance, although significant, is assumed to remain constant during translocation, as the DNA does not interfere with the field focusing outside the pore. For a typical case of $L_t \gg L \gg L_p$, where only the tail of the counter-ions is in the pore, the resistance inside the channel R_{channel} can be estimated

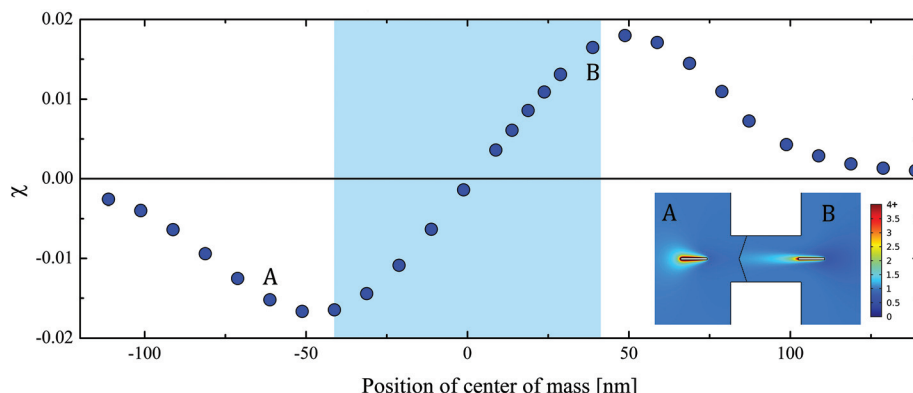


Fig. 3 FEM simulation of the ion current enhancement $\chi = \Delta I/I_0 = (I - I_0)/I_0$ during a nanopore translocation event as a function of the DNA center of mass from the pore center z_{cm} . I_0 is the baseline current without DNA ($r_p = 20 \text{ nm}$, $L_p = 60 \text{ nm}$, $L = 22.44 \text{ nm}$, $V = 10 \text{ V}$, $C_\infty = 0.01 \text{ M}$, $a = 1.185 \text{ nm}$, $\Sigma = 0.0275 \text{ C m}^{-2}$ and uncharged pore walls). The colored area corresponds to instances when DNA is in the pore. The negative resistive pulse maximum occurs when it has exited.

through $\int_0^{L_p} \frac{dz}{\sigma_p \pi r_p^2 + \left(\frac{FD}{RT} \right) \int_0^{2\pi} \int_0^{+\infty} \rho(r, z+L) r dr d\theta}$, where σ_p is

the solution conductivity of the uncharged pore $\sigma_p = 2C_\infty(F^2D/RT)$. As the co-ions have migrated in the direction away from the tail, the space charge density within the tail is close to the concentration of the extra counter-ions and hence will be used to estimate the conductance change. The azimuthal area integral of the space charge density in (7) represents the charge per unit length at the tail of the DNA and hence the differential conductance or inverse resistance. The net space charge in the tail is just the space charge of the DNA that has migrated downstream, $q_p - q_s$, and this integral can be approximated by $(q_p - q_s)/L_t$. For high fields, the channel resistance can hence

be simplified to $R_{\text{channel}} \approx \frac{L_p}{\sigma_p \pi r_p^2 + \left(\frac{FD}{RT} \right) \left(\frac{q_p - q_s}{L_t} \right)}$.

Therefore, the ion current enhancement degree at the end of a biphasic translocation, when only the tail is in the pore, can be

estimated through $\chi = \frac{\Delta I}{I_0} = \left(\frac{L_p}{\sigma_p \pi r_p^2} - R_{\text{channel}} \right) / R$, where I_0 is the baseline current and $\Delta I = I - I_0$ is the difference between the current measured at the end of the translocation event and the baseline. Therefore, if the number of charge carriers inside the pore is much larger than the number of counter-ions brought by the DNA, the enhancement degree can be approximated through $\chi \sim \left(\frac{2L_p}{\pi r_p} \right) \left(\frac{FD}{RT} \right) \left(\frac{q_p - q_s}{L_t} \right) / (\sigma_p \pi r_p^2 + 2\sigma_p r_p L_p)$.

Finally, using our expressions for q_s and L_t , the amplitude of the negative resistive pulse for the biphasic signal is

$$\chi \sim \left(\frac{2L_p}{\pi r_p} \right) \left[\frac{\left(\frac{FD}{RT} \right) \left(\frac{q_p}{PeL} \right) \left(\frac{L}{\lambda_D} \right)^2}{\sigma_p \pi r_p^2 + 2\sigma_p r_p L_p} \right] = \left(\frac{q_p}{2FC_\infty LA_p} \right) \left(\frac{L}{\lambda_D} \right)^2 Pe^{-1}, \quad (8)$$

where A_p is the area parameter related to the pore, $A_p = \pi r_p [\pi r_p^2 + 2r_p L_p]/2L_p$. This asymptotic approximation of the amplitude of the negative resistive pulse fits the numerically evaluated values of χ in Fig. 4(B) with a universal pre-factor of ≈ 1.5 . It decreases with the electric field by Pe^{-1} , as the space charge density in the tail decreases as Pe^{-1} along a cylinder of radius a .

This tail induced negative resistance pulse also explains the linear χ scaling in Fig. 3 when the tail is within the pore. Since the high field region exists only within or close to the nanopore, the tail exists only when the DNA is within some distance from the nanopore and its length is much longer than the pore length. During this interval, the ionic strength of the elongated tail is roughly constant and the amount of ions that is deposited within the pore is a linear function of the length of the tail within the pore. Outside this region, the tail is not fully formed and the usual Boltzmann–Debye layer, with exponential decay of the ionic strength with respect to distance, is responsible for the decay under bulk conditions ($\chi = 0$) as shown in Fig. 3.

Eqn (8) represents the high- Pe limit. Obviously, without field distortion, χ approaches zero and the low- Pe limit should also vanish, suggesting an optimum field strength (Pe) where the amplitude of the biphasic signal exhibits a maximum. Our numerical study does reproduce this optimum Pe , as shown in Fig. 4(A). The reported experimental data for χ are consistent with our numerical data but are on the left side of the optimum, showing a stronger biphasic amplitude with increasing applied field. According to (7), the optimum Peclet number should be $Pe(\lambda_D/L)^2 \sim O(1)$ and is hence larger for higher ionic strengths. This is qualitatively consistent with the simulated data and represents a new prediction for the maximum biphasic signal that has not been reported in earlier theoretical studies of biphasic signals for DNAs or nanoparticles. Note that if the removal of the positive resistive pulse is desired, as it may camouflage the information-rich negative resistive pulse, it would be sufficient to operate away from this Peclet number. The Peclet number can still be large so that the high-throughput feature of solid-state nanopores can still be retained for DNA translocation.

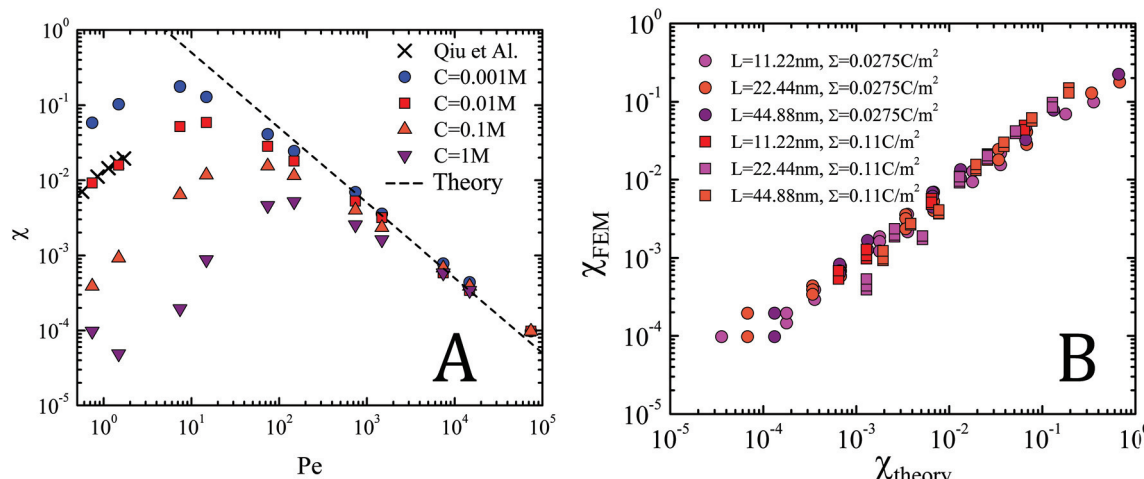


Fig. 4 (A) Ion current enhancement χ as a function of Pe both from FEM simulations ($L = 22.44 \text{ nm}$, $\Sigma = 0.0275 \text{ C m}^{-2}$, $C_\infty = 0.001, 0.01, 0.1$ and 1 M) and experiments on spherical colloids⁶ (crosses, $C_\infty = 0.1 \text{ M}$, L is the diameter of the colloid). (B) Comparison of our theoretical χ (5) with those obtained from FEM simulations. $C_\infty \in \{0.0001, 0.001, 0.01, 0.1\} \text{ M}$. All results presented in (B) satisfy $Pe(\lambda_D/L)^2 \gg 1$ ($L_p = 60 \text{ nm}$, $r_p = 20 \text{ nm}$, and $a = 1.185 \text{ nm}$).

Conclusions

We report the first theory for the biphasic ionic current signal, an important ion current fluctuation during DNA and nanoparticle translocation through solid-state nanopores. Our theory yields data that are consistent with numerical, MD and experimental data. We attribute the lagging negative resistive pulse in the biphasic signal to the intra-pore ion enrichment by counter-ions shed from the DNA by the electric shear, which then forms a comet-like structure (with a long tail) to the molecule. We also predict the existence of an optimal Peclet number or dimensionless applied field/DNA speed where this peak has the maximum amplitude. This maximum occurs because of a balance between the opposite dependence of the tail length and tail ionic strength with respect to the applied field, both of which contribute to the negative resistive pulse. This information can be used to better determine the size and zeta potentials of nanoparticles like exosomes,²³ differentiating unhybridized ssDNA from their duplexes by their mobility differences² and deciphering blocking molecules on a DNA for memory reading²⁴ and other potential solid-state nanopore applications in biotechnology. As the biphasic signal is also accompanied by a drastic change in the DNA or nanoparticle electrophoretic mobility, this study can also lead to more selective design of ion-selective membranes for electrodialysis in medical and waste treatment applications.^{25,26}

Methods

MD and FEM protocols

All finite-element simulations were performed in COMSOL 5.3a²⁷ using the coupled Multiphysics modules of electrostatics and transport of diluted species. Molecular dynamics simulations were performed in NAMD²⁸ with the CHARMM36 force field.²⁹ To

obtain a more proper characterization of the interaction between the charged and hydrophobic groups of DNA, the CUFIX modification of the CHARMM force field was implemented.³⁰

Considering the FEM simulation results in Fig. 2, different cylindrical particles with surface charge densities $\Sigma \in \{0.0275, 0.055, 0.11, 0.22\} \text{ C m}^{-2}$, lengths $L \in \{5.61, 11.22, 22.44, 33.66, 44.88\} \text{ nm}$ and radii $a \in \{1.185, 2.37, 5.925\} \text{ nm}$ were immersed in the axis of a 2D axial-symmetric geometry (cylinder) with a length of 120 nm and a radius of 80 nm. The solvent used was KCl and the ionic strength was varied from 0.1 mM to 1 M. The relative permittivity of the electrolyte ϵ is 80. A voltage drop was imposed between the inlet and outlet of the simulation domain, leading to field amplitudes E_∞ which were varied from 8 kV m^{-1} to 8 V nm^{-1} . The coupled Poisson-Nernst-Planck (PNP) partial differential equations were solved and an extra advective term was added into the dynamics of the ions, equivalent to imposing a referential that moves along with the particle at a velocity $\mu_p E_\infty$, where μ_p was considered as $10^{-9} \text{ ms V}^{-1} \text{ s}^{-1}$. The diffusion coefficient of both ions was calculated as $D = 2 \times 10^{-9} \text{ m}^2 \text{ s}^{-1}$, leading to a mobility $D/RT \gg \mu_{\text{DNA}}$. The charge in the surrounding of the cylindrical particle was estimated by integrating $Fz(C_+ - C_-)$ along the length of the particle from the surface of the particle to the surface of the box. In total 35 402 axisymmetric triangular elements with 18 051 vertices are used for the simulations. The mesh is refined near the edges of the cylindrical molecule to capture the boundary layer.

Considering the MD simulations shown in Fig. 2, a single double-stranded DNA molecule (TAGCTATCAGACTGATGTTGA) was immersed in a TIP-3P explicit water box³¹ of dimensions $60 \times 15 \times 15 \text{ nm}^3$. Potassium ions were placed by calculating the coulombic potential due to the DNA molecule in the nearby volume and the ions were placed at points of minimal energy using the cionize plugin of VMD.³² After this placement, sufficient potassium and chlorine ions were added to

the solution in order to obtain the desired molar strengths ($\{0.01, 0.05, 0.1, 0.5, 1\}$ M). The systems were equilibrated for 10 ns. For the first 9 nanoseconds, the counter-ions were held close to the DNA molecule and the axis of the molecule was held in the longest direction of the water box. During the last nanosecond, both the molecule and ions were left free to diffuse. After this equilibration, external electric fields were imposed in the longest direction of the box during 10 ns, with amplitudes $E_\infty \in \{0.01, 0.02, 0.04, 0.08, 0.1, 0.2, 0.4, 0.6, 1\}$ V nm $^{-1}$. The temperature of the system was held constant at 295 K using a Langevin thermostat with a damping frequency of 1 THz. A Nose–Hoover Langevin piston was applied to maintain the pressure at 1.01325 bar. A time-step of 2 fs was considered, and outputs of the trajectory were saved every 5000 steps. A distance cutoff of 12.0 Å was applied to short-range, non-bonded interactions, and 10.0 Å for the smothering functions. The charge in the surrounding of the DNA molecule was estimated by subtracting the total number of chlorine ions from the total number of potassium ions inside a cylinder that extends 3 nm in the radial direction beyond the radius of the DNA. The direction of the electric field is considered as the axis of the cylinder and the top and bottom bases are located at the top and bottom of the molecule. The charge in the surrounding of the molecule is fitted with an exponential decaying function $y_0 + Ae^{-t/\tau}$, where y_0 is the value considered for q_s .

As shown in Fig. 3 and 4, different cylindrical particles with surface charge density $\Sigma = 0.0275$ and 0.11 C m $^{-2}$, lengths $L \in \{11.22, 22.44, 33.66\}$ nm and radii $a = 1.185$ nm were immersed in the axis of a nanopore of radius $r_p = 20$ nm and length $L_p = 60$ nm built inside a 2D axial-symmetric geometry (cylinder) with a length of 460 nm and a radius of 200 nm. The solvent used was KCl and the ionic strength was varied from 0.1 mM to 1 M. The relative permittivity of the electrolyte ϵ is 80. A voltage drop was imposed between the inlet and outlet of the simulation domain, leading to field amplitudes E_∞ which were varied from 8 kV m $^{-1}$ to 8 V nm $^{-1}$. The coupled Poisson–Nernst–Planck (PNP) partial differential equations were solved with zero charge and no flux along the nanopore and cylinder walls and fixed concentrations of C_∞ at the upper and lower walls of the box. No flux is also imposed on the walls of the DNA molecule. The diffusion coefficient of both ions was calculated as $D = 2 \times 10^{-9}$ m 2 s $^{-1}$. The DNA molecule was moved along the axis of the box in increments of 5 nm (1 nm when the molecule is either partially or completely inside the pore) and the ionic current is measured in each step by integrating the current density $i = F^2 E(C_+ + C_-)(D/RT) - FD(\nabla C_+ - \nabla C_-)$ along the cross section of the pore. In total 160 113 axisymmetric triangular elements with 81 864 vertices are used for the simulations. The mesh is refined near both the edges of the molecule and the nanopore to capture the BL.

Conflicts of interest

There are no conflicts to declare.

Acknowledgements

SS and HCC are partially supported by NIHR21CA206904. ZP acknowledges the support from the National Science Foundation (No. 1706436-CBET). This work used the Extreme Science and Engineering Discovery Environment (XSEDE³³), of the NSF ACI-1548562 through Allocation No. TG-MCB180016. The authors acknowledge the Texas Advanced Computing Center (TACC) at The University of Texas at Austin for providing HPC resources that have contributed to the research results reported within this paper.

References

- R. M. Smeets, U. F. Keyser, D. Krapf, M.-Y. Wu, N. H. Dekker and C. Dekker, Salt dependence of ion transport and DNA translocation through solid-state nanopores, *Nano Lett.*, 2006, **6**(1), 89–95.
- A. Egatz-Gomez, C. Wang, F. Klacsmann, Z. Pan, S. Marczak, Y. Wang, G. Sun, S. Senapati and H.-C. Chang, Future microfluidic and nanofluidic modular platforms for nucleic acid liquid biopsy in precision medicine, *Biomicrofluidics*, 2016, **10**(3), 032902.
- S. Ghosal, J. D. Sherwood and H.-C. Chang, Solid-state nanopore hydrodynamics and transport, *Biomicrofluidics*, 2019, **13**(1), 011301.
- J. Menestrina, C. Yang, M. Schiel, I. Vlassiuk and Z. S. Siwy, Charged particles modulate local ionic concentrations and cause formation of positive peaks in resistive-pulse-based detection, *J. Phys. Chem. C*, 2014, **118**(5), 2391–2398.
- H. Wu, H. Liu, S. Tan, J. Yu, W. Zhao, L. Wang and Q. Liu, The estimation of field-dependent conductance change of nanopore by field-induced charge in the translocations of aunps-dna conjugates, *J. Phys. Chem. C*, 2014, **118**(46), 26825–26835.
- Y. Qiu, C. Yang, P. Hinkle, I. V. Vlassiuk and Z. S. Siwy, Anomalous mobility of highly charged particles in pores, *Anal. Chem.*, 2015, **87**(16), 8517–8523.
- Y. Qiu, C.-Y. Lin, P. Hinkle, T. S. Plett, C. Yang, J. V. Chacko, M. A. Digman, L.-H. Yeh, J.-P. Hsu and Z. S. Siwy, Highly charged particles cause a larger current blockage in micropores compared to neutral particles, *ACS Nano*, 2016, **10**(9), 8413–8422.
- K. Chen, N. A. Bell, J. Kong, Y. Tian and U. F. Keyser, Direction-and salt-dependent ionic current signatures for dna sensing with asymmetric nanopores, *Biophys. J.*, 2017, **112**(4), 674–682.
- S. Das, P. Dubsky, A. van den Berg and J. C. Eijkel, Concentration polarization in translocation of dna through nanopores and nanochannels, *Phys. Rev. Lett.*, 2012, **108**(13), 138101.
- A. Aksimentiev, Deciphering ionic current signatures of dna transport through a nanopore, *Nanoscale*, 2010, **2**(4), 468–483.

- 11 C. Wang, Q. Fu, X. Wang, D. Kong, Q. Sheng, Y. Wang, Q. Chen and J. Xue, Atomic layer deposition modified track-etched conical nanochannels for protein sensing, *Anal. Chem.*, 2015, **87**(16), 8227–8233.
- 12 J. Mathe, H. Visram, V. Viasnoff, Y. Rabin and A. Meller, Nanopore unzipping of individual DNA hairpin molecules, *Biophys. J.*, 2004, **87**(5), 3205–3212.
- 13 A. F. Sauer-Budge, J. A. Nyamwanda, D. K. Lubensky and D. Branton, Unzipping kinetics of double-stranded DNA in a nanopore, *Phys. Rev. Lett.*, 2003, **90**(23), 238101.
- 14 S. J. Fleming, B. Lu and J. A. Golovchenko, Charge, diffusion, and current fluctuations of single-stranded DNA trapped in an MspA nanopore, *Biophys. J.*, 2017, **112**(2), 368–375.
- 15 K. Chakraborty, P. Khatua and S. Bandyopadhyay, Exploring ion induced folding of a single-stranded DNA oligomer from molecular simulation studies, *Phys. Chem. Chem. Phys.*, 2016, **18**(23), 15899–15910.
- 16 D. R. Jacobson, D. B. McIntosh, M. J. Stevens, M. Rubinstein and O. A. Saleh, Single-stranded nucleic acid elasticity arises from internal electrostatic tension, *Proc. Natl. Acad. Sci. U. S. A.*, 2017, **114**(20), 5095–5100.
- 17 U. F. Keyser, B. N. Koeleman, S. Van Dorp, D. Krapf, R. M. Smeets, S. G. Lemay, N. H. Dekker and C. Dekker, Direct force measurements on DNA in a solid-state nanopore, *Nat. Phys.*, 2006, **2**(7), 473.
- 18 G.S. Manning, The molecular theory of polyelectrolyte solutions with applications to the electrostatic properties of polynucleotides, *Q. Rev. Biophys.*, 1978, **11**(2), 179–246.
- 19 A. S. Khair, Strong deformation of the thick electric double layer around a charged particle during sedimentation or electrophoresis, *Langmuir*, 2017, **34**(3), 876–885.
- 20 S. Sensale, Z. Peng and H.-C. Chang, Acceleration of dna melting kinetics using alternating electric fields, *J. Chem. Phys.*, 2018, **149**(8), 085102.
- 21 H.-C. Chang and L. Yeo, *Electrokinetically driven microfluidics and nanofluidics*, Cambridge University Press, 2010.
- 22 C. Lee, L. Joly, A. Siria, A.-L. Biance, R. Fulcrand and L. Bocquet, Large apparent electric size of solid-state nanopores due to spatially extended surface conduction, *Nano Lett.*, 2012, **12**(8), 4037–4044.
- 23 A. N. Boing, E. van der Pol, A. E. Grootemaat, F. A. Coumans, A. Sturk and R. Nieuwland, Single-step isolation of extracellular vesicles by size-exclusion chromatography, *J. Extracell. Vesicles*, 2014, **3**(1), 23430.
- 24 S. Wei and Z. Williams, Rapid Short-Read Sequencing and Aneuploidy Detection Using MinION Nanopore Technology, *Genetics*, 2016, **202**(1), 37–44.
- 25 Z. Slouka, S. Senapati and H.-C. Chang, Microfluidic Systems with Ion-Selective Membranes, *Annu. Rev. Anal. Chem.*, 2014, **7**, 317.
- 26 M. Elimelech and W. A. Phillip, The Future of Seawater Desalination: Energy, Technology, and the Environment, *Science*, 2011, **333**(6043), 712–717.
- 27 COMSOL Multiphysics® v.5.3a <http://www.comsol.com> COMSOL AB, Stockholm, Sweden.
- 28 J. C. Phillips, R. Braun, W. Wang, J. Gumbart, E. Tajkhorshid, E. Villa, C. Chipot, R. D. Skeel, L. Kale and K. Schulten, Scalable molecular dynamics with NAMD, *J. Comput. Chem.*, 2005, **26**(16), 1781–1802.
- 29 J. Huang and A. D. MacKerell Jr., CHARMM36 all-atom additive protein force field: Validation based on comparison to NMR data, *J. Comput. Chem.*, 2013, **34**(25), 2135–2145.
- 30 J. Yoo and A. Aksimentiev, Refined Parameterization of Nonbonded Interactions Improves Conformational Sampling and Kinetics of Protein Folding Simulations, *J. Phys. Chem. Lett.*, 2016, **7**(19), 3812–3818.
- 31 W. L. Jorgensen, J. Chandrasekhar, J. D. Madura, R. W. Impey and M. L. Klein, Comparison of simple potential functions for simulating liquid water, *J. Chem. Phys.*, 1983, **79**(2), 926–935.
- 32 W. Humphrey, A. Dalke and K. Schulten, VMD: visual molecular dynamics, *J. Mol. Graphics*, 1996, **14**(1), 33–38.
- 33 J. Towns, T. Cockerill, M. Dahan, I. Foster, K. Gaither, A. Grimshaw, V. Hazlewood, S. Lathrop, D. Lifka, G. D. Peterson, et al., Xsede: accelerating scientific discovery, *Comput. Sci. Eng.*, 2014, **16**(5), 62–74.